Calibration of an airborne HO_X instrument using the All Pressure Altitude based Calibrator for HO_X Experimentation (APACHE)

Daniel Marno[1], Cheryl Ernest[1*], Korbinian Hens[1**], Umar Javed[1,2], Thomas Klimach[1], Monica Martinez[1], Markus Rudolf[1], Jos Lelieveld[1], and Hartwig Harder[1]

[1] Atmospheric Chemistry Department, Max Planck Institute for Chemistry, 55128, Mainz, Germany
[2] Forschungszentrum Jülich GmbH, IEK-8, 52425, Jülich, Germany
*now at: Department of Neurology, University Medical Center of the Johannes Gutenberg University Mainz, 55131, Mainz, Germany
**now at: Hübner GmbH & Co KG – Division Hübner Photonics, 34123 Kassel, Germany

Correspondence: Daniel Marno (daniel.marno@mpic.de), Hartwig Harder (hartwig.harder@mpic.de)

Abstract. Laser induced fluorescence (LIF) is a widely used technique for both laboratory-based and ambient atmospheric chemistry measurements. However, LIF instruments require calibrations in order to translate instrument response into concentrations of chemical species. Calibration of LIF instruments measuring OH and HO_2 (HO_X), typically involves the photolysis of water vapor by 184.9 nm light thereby producing quantitative amounts of OH and HO_2. For ground-based systems HO_X instruments, this method of calibration is done at one pressure (typically ambient pressure) at the instrument inlet. However, airborne HO_X instruments can experience varying cell pressures, internal residence times, temperatures, and humidity during flight. Therefore, replication of such variances when calibrating are essential to acquire the appropriate sensitivities. This requirement resulted in the development of the APACHE (All Pressure Altitude-based Calibrator for HO_X Experimentation) chamber. It utilizes photolysis of water vapor, but has the additional ability to alter the pressure at the inlet of the HO_X instrument thus relating instrument sensitivity to the external pressure ranges experienced during flight (275 to 1000 mbar). Measurements supported by COMSOL multiphysics and its computational fluid dynamics calculations revealed that, for all pressures explored in this study, APACHE is capable of initializing homogenous flow and maintain near uniform flow speeds across the internal cross-section of the chamber. This reduces the uncertainty regarding average exposure times across the mercury (Hg) UV ring lamp. Two different actinometrical approaches characterized the APACHE UV ring lamp flux as 6.3 x 10^{14} ($\pm$ 0.9 x 10^{14}) s^{-1} depending on pressure. Data presented in this study are the first direct calibrations, performed in a controlled environment using APACHE of an airborne HO_X system instrument.

1 Introduction

It is well known that the hydroxyl (OH) radical is a potent oxidizing agent in daytime photochemical degradation of pollutants sourced from anthropogenic and biogenic processes thus accelerating their removal from our atmosphere. The hydroperoxyl radical (HO_2) also plays a central role in atmospheric oxidation as it not only acts as a reservoir for OH, but is involved in formation of other oxidants such as peroxides and impacts the cycling of pollutants such as NO_X (= NO + NO_2) (Lelieveld et al., 2002). Therefore, measurements of OH and HO_2 (HO_X) within the troposphere are essential in understanding the potential global scale impacts of pollutants in both the present day and in climate predictions. One common HO_X measurement method is Laser Induced Fluorescence (LIF) (Stevens et al., 1994; Brune et al.,

46 1995; Hard et al., 1995; Martinez et al., 2003; Faloona et al., 2004; Hens et al., 2014; Novelli
47 et al., 2014). However, other methods have been successfully implemented to measure HO_X.
48 Chemical Ionization Mass Spectrometry (CIMS) (Sjostedt et al., 2007; Dusanter et al., 2008;
49 Kukui et al., 2008; Albrecht et al., 2019) and Differential Optical Absorption Spectroscopy
50 (DOAS) (Brauers et al., 1996; Brauers et al., 2001; Schlosser et al., 2007) have also been used
51 in the measurement of HO_X in the field and in intercomparison projects with LIF
52 instrumentation. However, low atmospheric concentrations of HO_X (Schlosser et al., 2009) and
53 potential interferences (Faloona et al., 2004; Fuchs et al., 2011; Mao et al., 2012; Hens et al.,
54 2014; Novelli et al., 2014; Fuchs et al., 2016) can make HO_X measurements especially
55 challenging. Airborne LIF-FAGE (LIF-Fluorescence Assay by Gas Expansion) instruments
56 experience large variability in pressure, humidity, instrument internal air density, and internal
57 quenching during flights, which cause a wide array of instrumental sensitivities (Faloona et al.,
58 2004; Martinez et al., 2010; Regelin et al., 2013; Winiberg et al., 2015). Therefore, it is critical
59 to utilize a calibration system that can suitably reproduce in-flight conditions to determine the
60 instrument response to known levels of OH and HO_2 to acquire robust HO_X measurements.
61 The first stage of the our Hydroxyl Radical measurement Unit based on fluorescence
62 Spectroscopy (HORUS) inlet is an inlet pre-injector (IPI), used to determine the concentration
63 of background OH interferences by removing atmospheric OH from the signal via addition of
64 an OH scavenger such as propane. IPI draws 50-230 sL min^{-1} depending on altitude and is
65 susceptible to temperature and pressure-driven changes in internal reaction rates and residence
66 times under flight conditions. This has implications for the removal of atmospheric OH in the
67 inlet and for the characterization of background interference signals in HORUS. Therefore, a
68 device capable of providing stable high flows whilst reproducing a wide range of pressures and
69 temperatures is needed in order to calibrate the airborne HORUS instrument.

70

2   Experimental design and set up

72

2.1 APACHE design overview

74

75   Figure 1 shows the overview of the APACHE system. In front of the APACHE inlet, a series
76 of mixing blocks were installed where multiple dry synthetic air additions were injected into a
77 controlled humidified air supply ensuring thorough mixing of water vapor before being
78 measured by a LI-COR 6262 CO_2/H_2O (figure 1a). This air is then fed into a large mass flow
79 controller (MFC). The construction of the APACHE chamber itself is shown in figure 1b. The
80 first section contains the diffuser inlet with a sintered filter (bronze alloy, Amtag, filter class
81 10). This 2 mm thick sintered filter, with a pore size of 35 μm, which initializes a homogeneous
82 flow and further improves the mixing of water vapor before passing over the UV ring lamp
83 (described further in section 4). The water photolysis section contains a low-pressure, 0.8 A,
84 mercury ring lamp (uv-technik, see supplementary, figure S.1) which produces a constant radial
85 photon flux at 184.9 nm, situated 133 mm after the sintered filter and separated from the main
86 APACHE chamber by an airtight quartz window. Between the lamp and the quartz window
87 there is an anodized aluminum band with thirty 8 mm apertures, which blocks all light apart
88 from that going through the apertures, which reduces the amount of UV flux entering APACHE
89 and controls the size of the illuminated area. The HORUS inlet is clamped down 169.5 mm
90 after the photolysis section in such a way that the instrument sample flow is perpendicular to
91 the airflow passing over the inlet. The inlet protrudes 51.5 mm into the APACHE cavity much
92 like it is when installed in the aircraft shroud system (see figure 2), and is made air tight with
93 the use of O-rings. Opposite the HORUS inlet, there is an airtight block attachment containing
94 a series of monitoring systems.
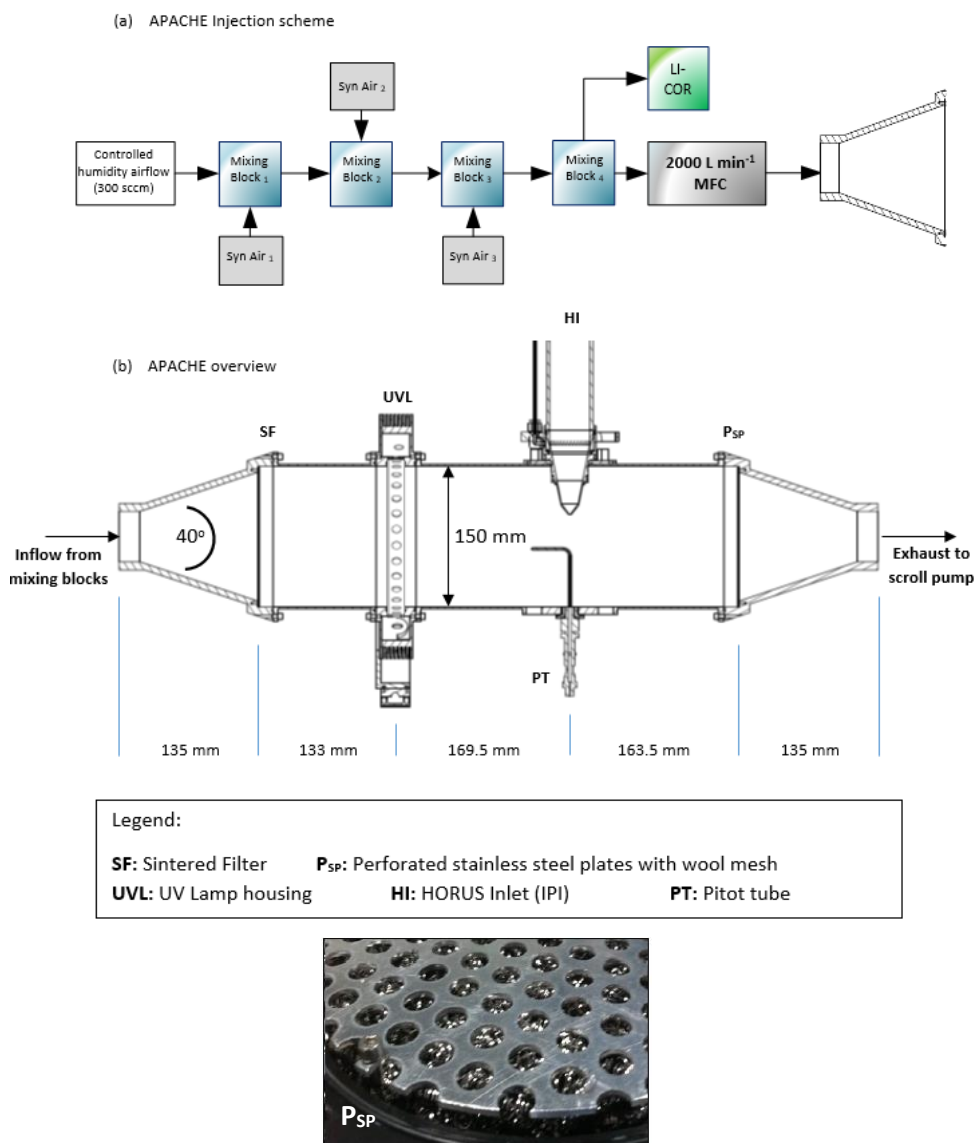
Figure 1. Overview of the APACHE system and the pre mixing set up. With a picture of perforated stainless steel plates with wool mesh.

95

96   One system being a pitot tube attached to an Airflow PTSX-K 0-10Pa differential pressure
97   sensor (accuracy rating of 1% at full scale, 1σ), which is used to monitor the internal flow
98   speeds within APACHE. A 3 kOhm NTC-EC95302V thermistor is used to monitor the air
99   temperature and an Edwards ASG2-1000 pressure sensor (with an accuracy rating of $\pm$ 4 mbar,
100   2σ) monitors the static air pressure. Additionally, there are two one-quarter inch airtight
101   apertures in the monitoring block that can be opened to enable other instrumentation to be
102   installed.

2.2 Pressure control

For this study, the operational pressure range of APACHE used was 250 – 900 mbar, with precision of $\pm$ 0.1% (1σ) and accuracy of $\pm$ 2% (1σ) with mass flows ranging from 200 to 990 sL min^{-1}. This was achieved by an Edwards GSX160 scroll pump controlling the volume flow, which resulted in air speeds of 0.9 to 1.5 m s^{-1} through APACHE at 250 and 1000 mbar respectively at 25 °C, used in combination with a MFC (Bronkhorst F-601A1-PAD-03-V) capable of controlling a mass flow of up to 2000 sL min^{-1} dictating the mass flow of air entering APACHE and thus controlling the pressure. Although not critical for this study, the operational pressure range of APACHE can be extended by changing the draw speed of the Edwards scroll pump. However, that may cause the flow speeds and potentially the flow speed profiles across the UV ring lamp to vary in between different pressure calibrations.

2.3 The airborne HORUS instrument

The LIF-FAGE instrument developed by our group (HORUS), is based on the original design of GTHOS (Ground Tropospheric Hydrogen Oxide Sensor) described by Faloona et al. (2004) and is described in further detail by Martinez et al. (2010). The airborne instrument is a revised and altered design to perform under conditions experienced during flight and conform to aeronautical regulations. It was primarily developed for installation on the High Altitude and Long Range Research Aircraft (HALO). The system comprises of an external inlet shroud, detections axes, laser system, and a vacuum system (figure. 2). Additionally, this is the first airborne LIF-FAGE instrument measuring HO$_X$ with a dedicated inlet pre injector (IPI) system installed for the purpose of removing atmospheric OH enabling real time measurements and quantification of potential chemical background OH interferences. The airborne IPI system is redesigned to fit within the shroud inlet system, whilst maintaining similar operational features as the on-ground IPI installation (Novelli et al., 2014).

To prevent excessive collisions of OH and HO$_2$ with the IPI orifice and internal walls, thus limiting losses of HO$_X$, the momentum inertia of the air passing through the external shroud system had to be overcome to promote flow direction into the instrument. This was achieved by installing in the shroud a choke point behind the instrument inlet, resulting in air flow to decrease from ~ 200 to < 21 m s^{-1}, which is sufficiently below the sample velocity of HORUS (44 – 53 m s^{-1}). Additionally, it limits non-parallel flows across the HORUS inlet created by variable pitch, roll and yaw changes of the aircraft. As the aircraft changes pitch, roll and yaw, the measured OH variability increases by $\pm$ 4.51 x10^4 cm^{-3} (1σ), which is only 10 to 15 % higher than the natural variability of OH on average. This increase in variability is negligible as is represents, depending on internal pressure, 19 to 30 % of the detection limit of the instrument. Both these effects of the external shroud improve the measurement performance by reducing variable wall losses of HO$_X$ at the HORUS inlet under flight conditions.
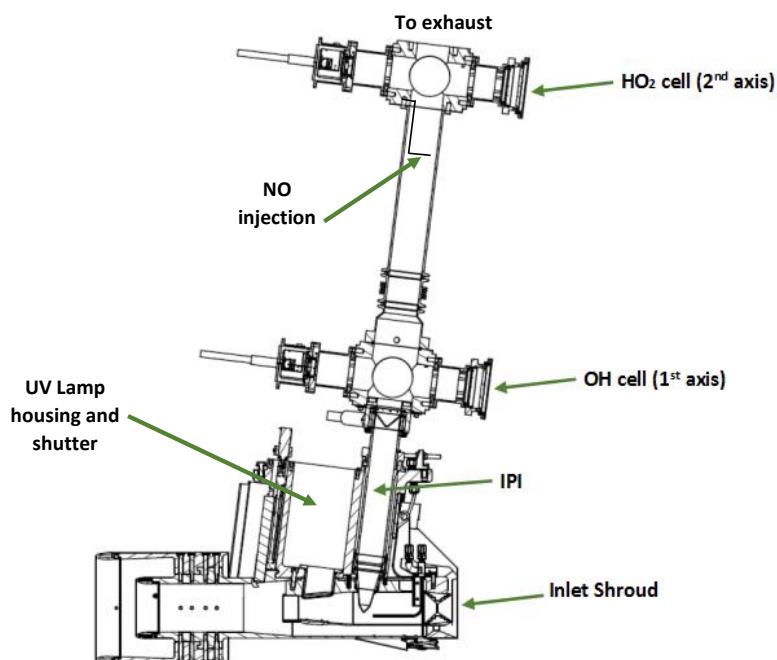
Figure 2. Overview of the airborne HORUS system as installed in the HALO aircraft. HO_2 is measured indirectly through the addition of NO that quantitatively converts HO_2 into OH. The NO injection occurs via a stainless steel 1/8 inch line, shaped into a ring perpendicular to the airflow with several unidirectional apertures of 0.25 mm diameter creating essentially a NO shower.

143

144 As with other LIF-FAGE HO_X instruments, HORUS measures an off-resonance signal to
145 discern the net OH fluorescence signal. This is achieved by successive cycling of the laser
146 tuning from on-resonance (measuring the total signal of OH fluorescence and the signal
147 originating from other fluorescence and electronic sources), to off-resonance (measuring all
148 the above except the OH fluorescence). The HORUS instrument utilizes the $Q_1(2)$ transition
149 $X^2\Pi_{3/2}(v''=0) \rightarrow A^2\Sigma^+(v'=0)$ (Dorn et al., 1995; Holland et al., 1995; Mather et al., 1997).
150 The net OH signal (S_{OH}) is thus the difference between the on-resonance and off-resonance
151 signals. The OH sensitivity (C_{OH}) and average laser power within the detection axis ($Wz_{1\ pwr}$)
152 are then used to calculate the absolute OH mixing ratio (see Eq. (1)). HO_2 is measured indirectly
153 through the quantitative conversion of atmospheric HO_2 to OH by injection of nitric oxide
154 (NO) under the low-pressure conditions within HORUS.

155

156 $HO_2 + NO \rightarrow NO_2 + OH$ (R1)

157

158 When NO is injected into the instrument, both ambient OH and HO_2 are measured in the
159 second detection axis. The net HO_2 signal (S_{HO2}) in the second axis is therefore derived from
160 subtracting the net OH signal from the first detection axis normalized by the ratio of the OH
161 sensitivities for the two detection axes ($C_{OH(2)}\ /\ C_{OH}$) from the net HO_X signal (S_{HOx}). Then
162 S_{HO2} is corrected by the sensitivity to HO_2 (C_{HO2}) and laser power ($Wz_{2\ pwr}$) to reach absolute
163 HO_2 mixing ratio (see Eq. (2)).

164 $\quad OH = \dfrac{S_{OH}}{(C_{OH} \cdot Wz_{1\,pwr})}$ (1)

165

166 $\quad HO_2 = \dfrac{1}{(C_{HO_2} \cdot Wz_{2\,pwr})} \cdot \left\{ S_{HO_x} - \dfrac{C_{OH(2)}}{C_{OH}} S_{OH} \right\}$ (2)

167

168 $Wz_{1\,pwr}$ is the laser power in the first detection axis, $Wz_{2\,pwr}$ is the laser power in the second
169 detection axis and C_{OH} and C_{HO2} are the calibrated sensitivity factors for OH and HO$_2$ (cts s^{-1}
170 pptv^{-1} mW^{-1}) respectively. By calibrating using a known OH mixing ratio, the instrument
171 sensitivity C_{OH} can be determined by rearranging Eq. (1) to:

172

173 $\quad C_{OH\,(cal)} = \left. S_{OH_{cal}} \middle/ (OH \cdot Wz_{1\,pwr}) \right.$ (3)

174 The sensitivity of HORUS depends on the internal pressure, water vapor mixing ratios, and
175 temperature, which are subject to change quite significantly during flight. Therefore, further
176 parameterization when calibrating is required to fully constrain the sensitivity response of the
177 instrument at various flight conditions. Eq. (4) shows the terms that affect the sensitivity of
178 the first HORUS axis that measures OH.

179 $\quad C_{OH}(P,T) = c0 \cdot \rho_{Int}(P,T) \cdot Q_{IF}(P) \cdot b_c(T) \cdot Wz_{pwr} \cdot [\alpha_{IPI}(P,T) \cdot \alpha_{HORUS}(P,T)]$ (4)

180 Where c0 is determined by calibrations and is the lump sum coefficient of all the pressure
181 independent factors affecting the HORUS sensitivity, for example, OH absorption cross section
182 at 308nm, the photon collection efficiency of the optical setup and quantum yield of the
183 detectors, as well as pressure independent wall loss effects (cts cm^3 molecule^{-1} s^{-1}). ρ_{Int} is the
184 internal molecular density. Q_{IF} is the quenching effect of N$_2$, O$_2$ and H$_2$O occurring inside the
185 detection axis, which is normalized to 1 % water mixing ratio. Both are pressure dependent
186 terms as denoted in Eq. (4). The Boltzmann correction (b_c) has a temperature dependency as
187 it corrects for any OH molecules that enter the HORUS instrument in a thermally excited state
188 and are therefore not measurable by fluorescence excitation at the wavelength used. Wz_{pwr} is
189 the measured laser power entering the white cell in the detection axis. α is the pressure
190 dependent OH transmission, which is the fraction of OH that reaches the point of detection.
191 This term is separated for the two-tier pressure conditions present in the instrument. The term
192 α_{IPI} represents the correction for pressure and temperature dependent OH loss on the walls
193 within IPI (post pinhole, pre-critical orifice). The term α_{HORUS} is the correction for pressure
194 dependent OH loss to the walls within the HORUS detection axes post critical orifice. Whilst
195 the quenching effects, internal densities and Boltzmann corrections can be quantified, and the
196 power entering the measurement cell is measured, the two factors that need to be determined
197 through calibration are c0 and OH transmission. Once the c0 coefficient and α terms are known,
198 the final in-flight measured OH mixing ratio (pptv) is found:

199 $\quad OH = \left. S_{OH} \middle/ (c0 \cdot \rho_{Int} \cdot Q_{IF} \cdot b_c \cdot Wz_{pwr} \cdot [\alpha_{IPI} \cdot \alpha_{HORUS}]) \right.$ (5)

200 As depicted in both figure 1b and figure 2, the complete system is calibrated with IPI
201 attached and operating as it did when installed in the aircraft. Therefore, the combined losses
202 of OH within IPI and in the low pressure regime post critical orifice contribute to the overall
203 calibrated C_{OH} sensitivity factor in the same way during measurement and calibrations,

204   meaning that the OH transmission of HORUS can be quantified with both OH transmission
205   terms (α_{IPI} and α_{HORUS}) combined into one term (α_{Total}).

206    $$OH = \left. S_{OH} \middle/ \left(c0 \cdot \rho_{Int} \cdot Q_{IF} \cdot b_c \cdot Wz_{pwr} \cdot [\alpha_{Total}] \right) \right. \qquad (6)$$

207   Figure 3 shows the graphical representation of the different factors described above and
208   their impact on the overall sensitivity.
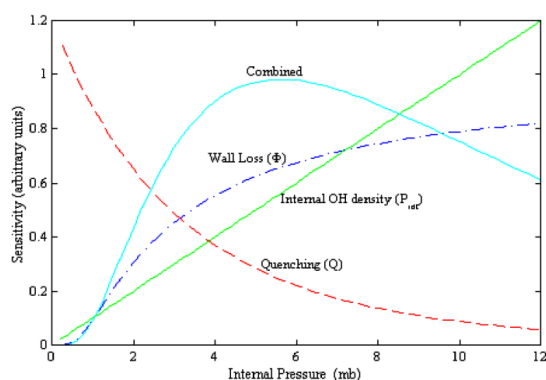
Figure 3. Pressure dependent components affecting LIF sensitivity. Internal density (solid green line), OH transmission (dotted blue line), and quenching (dotted red line). The product of these factors produce the expected pressure dependent sensitivity. (Modified after Faloona et al., 2004).

209

210   3   Calibration method and theory

211   As an overview, table 1 shows common calibration techniques for OH instruments. The
212   APACHE system is based on the production of known quantified and equal concentrations of
213   OH and HO_2 via photolysis of water vapor in pure synthetic air using a Hg ring lamp emitting
214   UV radiation at 184.9 nm.

215    $$H_2O + h\upsilon \xrightarrow{\lambda = 184.9 \text{ nm}} OH + H^* \qquad (R2)$$

216    $$H^* + O_2 \xrightarrow{O_2} OH + O_3 \qquad (R3)$$

217    $$H^* \xrightarrow{M} H \qquad (R4)$$

218    $$H + O_2 \xrightarrow{M} HO_2 \qquad (R5)$$

219   Stable water mixing ratios with a variability of $< 2 \%$ were achieved by heating 300 sL min^{-1}
220   flow of synthetic air to 353 K and introducing deionized water using a peristaltic pump into
221   this heated gas flow causing it to evaporate before entering a 15 L mixing chamber. This
222   prevents re-condensation and humidity spikes when the pump is introducing the water. The
223   humidified gas flow is then diluted (to around 3 mmol mol^{-1}) and mixed further with additional
224   dry pure synthetic air via a series of mixing blocks to achieve the required and desired stable
225   water vapor mixing ratios. The photolysis of H_2O has only one spin-allowed and energetically
226   viable dissociation channel at 184.9 nm (Engel et al., 1992), meaning the quantum yield of OH

227 and H* are unified (Sander et al., 2003). Even though reaction R3 is possible particularly since
228 the H* atoms can carry transitional energies of 0.7 eV at 189.4nm (Zhang et al., 2000), the fast
229 removal of energy by reaction R4 allows for the general assumption that all H * atoms produced
230 leads to HO_2 production. The use of water photolysis as a OH and HO_2 radical source for
231 calibration of HO_X instruments has been adopted in a number of studies (Heard and Pilling.
232 2003; Ren et al., 2003; Faloona et al., 2004; Dusanter et al., 2008; Novelli et al., 2014; Mallik
233 et al., 2018). As an example, the factors required to quantify the known concentrations of OH
234 and HO_2 during calibrations are shown below:

235 $$[OH] = [HO_2] = [H_2O] \cdot \sigma_{H_2O} \cdot F_{184.9\,nm} \cdot \phi_{H_2O} \cdot t \tag{7}$$

236 **Table 1.** Various known methods for OH instrument calibrations.

	Technique	Method	Quoted (1σ) Uncertainty	Limitations	References
(1)	Water UV-Photolysis	See section 3.1	10-30%	Dependent on lamp, photon flux measurement, and absorption	(Creasey et al., 2003; Heard and Pilling. 2003; Holland et al., 2003; Ren et al., 2003; Faloona et al., 2004; Smith et al., 2006; Martinez et al., 2010; Mallik et al., 2018)
(II)	Pulsed N_2-H_2O RF discharge	At low pressure (0.1 Torr); OH and NO produced using a low power RF discharge. Concentrations of NO and OH are closely linked	20%	Requires NO measurement using stable ambient air calibrations	(Dilecce et al., 2004; Verreycken and Bruggeman. 2014)
(III)	Low-pressure flow-tube RF discharge	OH radical production by titration of H atoms with NO_2. Known amount of H atoms produced using microwave discharge using low pressure flow tube	30%	Stable ambient air calibrations	(Stevens et al., 1994)
(IV)	Continuously Stirred Tank Reactor	In a CSTR, OH produced through UV-irradiation of specific Hydrocarbon in presence of H_2O and NO. concentration of OH relates to loss of the Hydrocarbon	36%	Time intensive, systematic wall loss of OH in reactor	(Hard et al., 1995; Hard et al., 2002)
(V)	Steady-State O_3-alkene	A steady state OH concentration produced from ozonolysis of a known concentration of an alkene	42%	Time consuming, large uncertainties compared to other methods	(Heard and Pilling. 2003; Dusanter et al., 2008)
(VI)	Laser photolysis of Ozone	Photolysis of O_3 with 284 nm light producing $O(^1D)$. Which then reacts with H_2O producing OH	40-50%	Requires large apparatus	(Tanner and Eisele. 1995)

237

238 Where in Eq. (7), the OH and HO_2 concentrations are a product of photolysis of a known
239 concentration of water vapor [H_2O], σ_{H2O} is the absorption cross section of water vapor, 7.22
240 ($\pm$ 0.22) x 10^{-20} cm^2 molecule^{-1} at 184.9 nm (Hofzumahaus et al., 1997; Creasey et al., 2000).

$F_{184.9\ nm}$ is the actinic flux (photons s^{-1}) of the mercury lamp used for photolysis, ϕ_{H2O} is the quantum yield and t is exposure time. The quantum yield of water vapor photolysis at the 184.9 nm band is 1 (Creasey et al., 2000).

4 APACHE conditions and parametrizations

4.1 Flow conditions

With any calibration device, the flow conditions must be characterized to inform subsequent methods and calibrations. Regarding APACHE, the two main factors to be resolved are (i) how uniform are the flow speed profiles and therefore exposure times in respect to the APACHE cross section, and (ii) the impact of OH wall losses.

To this end, experimental and model tests were performed to determine whether the combination of the sintered filter, and the stainless steel perforated plates and wool arrangement could provide a homogeneous flow. This means that under operation the flow speeds should be uniform along the cross section of APACHE to within the uncertainty of the measurements. This is to ensure that the air masses passing across the lamp have the same exposure times irrespective of where they are in the cross section. Additionally, model simulations can provide an indication of, as a function of APACHE pressure, the development and scale of boundary air conditions where air parcels experience extended contact time with the interior walls of APACHE, and so have pronounced OH wall losses. This highlights potential flow conditions where there is sufficient time between the photolysis zone and the HORUS inlet to allow APACHE boundary air to expand into and influence the OH content of the air being sampled by HORUS.

4.1.1 Flow speed profiles

During calibration, the pressures within the HORUS instrument had to be controlled and monitored to replicate the inflight conditions. The APACHE chamber pressure is equivalent to the inflight pressure in the shroud where the HORUS system samples. The pressure of the detection axes depends on the pressure at the inlet and the efficiency of the pumps. For IPI however, the airflow through it is dependent on the pressure gradient between the shroud and the ambient pressure at the IPI exhaust or alternatively the APACHE pressure and pressure in front of the XDS 35 scroll pump (post IPI blower). During the campaign, the exhausts of all blowers and pumps of the HORUS system were attached to the passive exhaust system of the aircraft and were thus exposed to ambient pressure. Therefore, in the lab and throughout the calibrations, the pressure at the exhaust for every blower and pump involved in the HORUS instrument was matched to the respective in-flight ambient pressures by attaching a separate pressure sensor, needle valve and XDS35 scroll pump system. Figure 4 shows the lab setup described above.
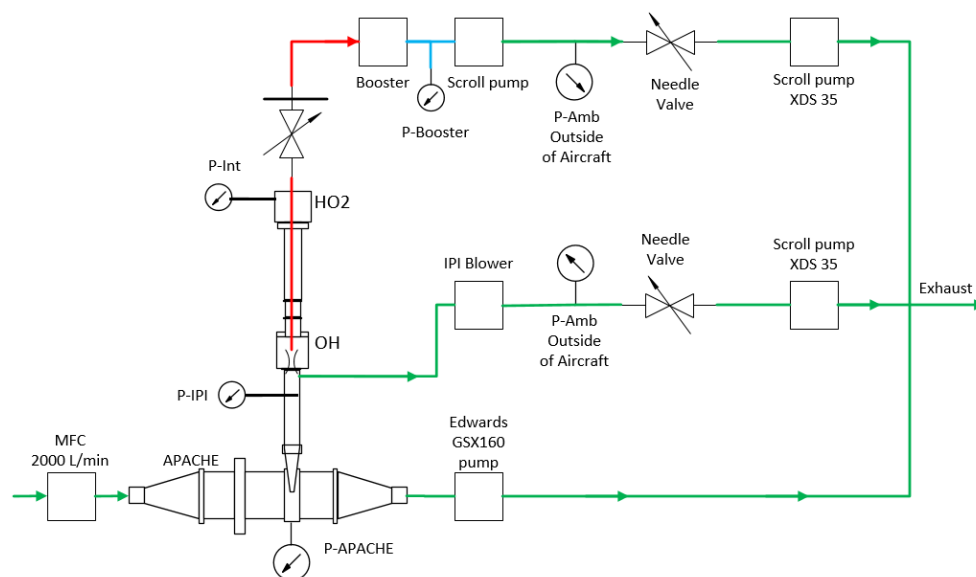
Figure 4. The experimental setup with the additional needle valves, pressure sensors and XDS35 scroll pumps attached to the exhausts of all pumps and blowers of HORUS to match in-flight pumping efficiencies when calibrating with APACHE. The red lines depict the low-pressure region within HORUS, the blue is the pressure monitoring line between the booster and scroll pump that drive the HORUS sample flow, and the green show the external gas lines.

280

281   To limit the effect of wall loss, HORUS samples air from the core of the APACHE flow system
282   and draws only a fraction of the total air flow as shown in figure 5. At 900 hPa the HORUS
283   instrument takes 20 % and at 275 hPa HORUS takes 30 % of the total volume flow entering
284   APACHE. To validate that this proportional volume flow into HORUS does not disturb the
285   flow conditions within APACHE, flow speed profiles were performed using the Prandtl pitot
286   tube installed directly opposite the HORUS inlet, which can be positioned flush against the
287   internal wall up to 60.5 mm into the APACHE cavity, which is 15 mm from the APACHE
288   center. Figure 6 shows the measured flow speed profile (blue data points) when the APACHE
289   pressure was 920 hPa. As the distance between the APACHE wall and the pitot tube inlet
290   increased, no significant change in the flow speed was observed. The largest change observed
291   was between 46.6 and 60.5 mm where the flow speed increased by 0.16 m s^{-1}, which is 22.8 %
292   smaller than the combined uncertainty of these two measurements $\pm$ 0.21m s^{-1} (2σ). Compared
293   to the other four measurement points performed at 920 mbar, the 1.54 m s^{-1} measured at 60.5
294   mm is not significantly different. However, when performing the speed profile tests at the low
295   pressures, the pressure difference measured was close to or below the resolution of the
296   differential pressure sensor. Consequently, the flow inside APACHE and the HORUS inlet
297   system was simulated using the computational fluid dynamics (CFD) model from COMSOL
298   multiphysics to gain a better understanding of the flow speed profiles at all pressures. The CFD
299   module in COMSOL uses Reynolds Averaged Navier-Stokes (RANS) models (COMSOL.
300   2019). The standard k-epsilon turbulence model with incompressible flows was used for this
301   study as it is applicable when investigating flow speeds below 115 m s^{-1} (COMSOL. 2019).
302   An extra fine gridded mesh of a perforated plate with a high solidity (σ$_s$ = 0.96) was
303   implemented in the turbulence model to generate the turbulence and replicate the flows created

304   by the bronze sintered filter (Roach. 1987). The model was constrained with the pressures
305   measured within APACHE and the HORUS inlet. The volume flow was calculated from
306   measured mass flow entering APACHE and temperatures were constrained using the
307   thermistor readings. To gain confidence in the model, the flow speed output data was compared
308   to the available measured flow speed profile, see figure 6. Overall, the modelled flow speed
309   profile did not differ significantly from measured. The only point where the model
310   significantly disagreed with measurements was at the boundary (< 4 mm away from the
311   APACHE wall), where the model predicted a flow speed of 1.3 m s^{-1}, which is 6 % lower than
312   the minimum extent of the measurement uncertainty 1.38 m s^{-1}. However, as this is occurring
313   within a region that ultimately does not influence the air entering HORUS, see section 4.1.2,
314   the disagreement between modelled and measured flow speeds at distances less than 4 mm
315   from the APACHE wall is ignored.
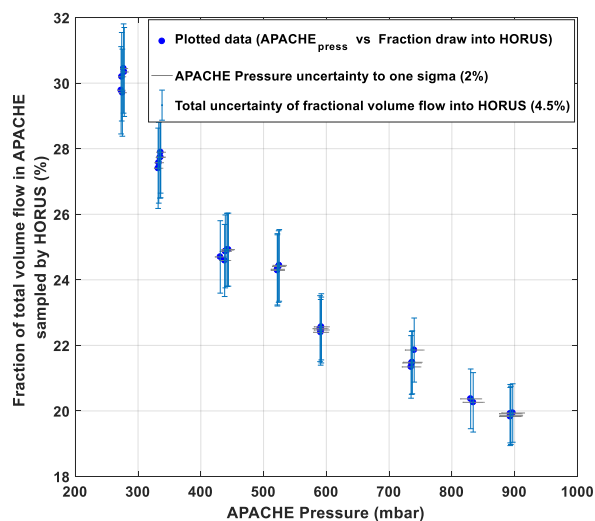
Figure 5. The percentage of the total volume flow entering APACHE, which is sampled by HORUS as a function of pressure within APACHE. All error bars are quoted to 1σ.
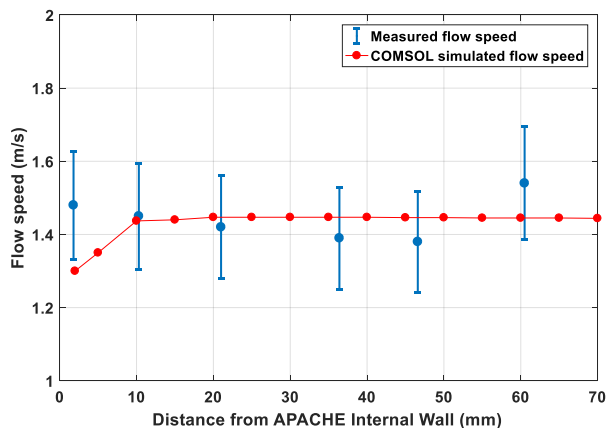
Figure 6. The measured (blue) and COMSOL simulated (red) flow speed profiles within APACHE, at 920 hPa. The x-axis is the distance from the internal wall of APACHE. The error bars are quoted to 2σ.

316 Figure 7 shows the simulated flow speeds at six discreet pressures within APACHE. The black
317 lines depict the streamlines of the HORUS sample flow and the color gradient relates to the
318 flow speed. The flow conditions in the center flow within the HORUS inlet, post pinhole, the
319 center of the streamlines and the undisturbed flow airflow not influenced by the sample flow
320 of HORUS are indicated. The figure shows the internal APACHE dimensions starting from the
321 sintered filter to the first perforated stainless steel plate 0.135 m and 0.601 m from the
322 APACHE inlet, respectively. From the simulations, the centerline flow speed differs by less
323 than 0.1 % compared to the undisturbed flow, which is also the case at 275 mbar when HORUS
324 is drawing in the highest percentage of the total volume flow entering APACHE. After the
325 sintered filter the high calculated Reynolds numbers (Re > 2300) support the statement that a
326 turbulent flow regime is created. Additionally, the measurements in conjunction with
327 simulations show that the small pores of the sintered filter release a uniform distribution of
328 small turbulent elements across the diameter of APACHE, which remain prevalent all the way
329 up to the HORUS inlet.

330

331 4.1.2 HOx losses in APACHE

332 The modelled OH mixing ratios (pptv) in figure 8 show the change in OH content as the air
333 flows along the length of APACHE. Mixing ratios were used as they are independent of the
334 changing density within APACHE. In every simulation, the OH and HO_2 concentrations were
335 initialized at zero, and losses at the walls were fixed to 100 % for both OH and HO_2. The radial
336 photolytic production of OH and HO_2 as calculated using Eq. (7) and Eq. (8), occurred when
337 the air passeed the UV ring lamp. For all simulations, the HO_X radical-radical recombination
338 loss reactions, (reactions R6-R8), and the measured molecular diffusion coefficient of OH_{Dm}
339 in air (Tang et al., 2014) was used:

340 OH_{Dm} = 179 (± 20) Torr cm^2 s^{-1} (238.65 ± 26.7 hPa cm^2 s^{-1})

341 In literature, there have been no reports of successfully performed tests that accurately
342 measure HO_2 diffusivity coefficients in air. However, calculations of HO_2 diffusion
343 coefficients using the Lennard-Jones potential model have been performed (Ivanov et al.,
344 2007). Ivanov et al. (2007) performed a series of measurements and Lennard-Jones potential
345 model calculations to quantify the polar analogue diffusion coefficients for OH, HO_2 and O_3 in
346 both air and pure helium. The calculated OH and O_3 diffusion coefficients in air from the
347 Lennard-Jones potential model were in good agreement with the recommended measurement
348 values in Tang et al., (2014) well within the given uncertainties. Therefore, to best replicate the
349 diffusivity of HO_2 within the simulations, the following diffusion coefficient of HO_2 in air from
350 the Ivanov et al., (2007) paper was used:

351 $HO_{2\ Dm}$ = 107.1 Torr cm^2 s^{-1} (142.8 hPa cm^2 s^{-1})

352 It is clear from figure 8, that irrespective of pressure the air masses at the boundary (where
353 wall losses are 100 %) do not have sufficient time to expand into the HORUS sample flow
354 streamlines, and influence HO_X content entering HORUS. Lateral exchanges between air at the
355 walls of APACHE and the free air in the center are suppressed due to the preservation of the
356 small turbulence regime between the sintered filter and the HORUS inlet. Table 2 provides, for
357 six pressures, the evolution of OH along the length of APACHE, within the streamlines created
358 by the HORUS sample flow as depicted in figure 8.

359
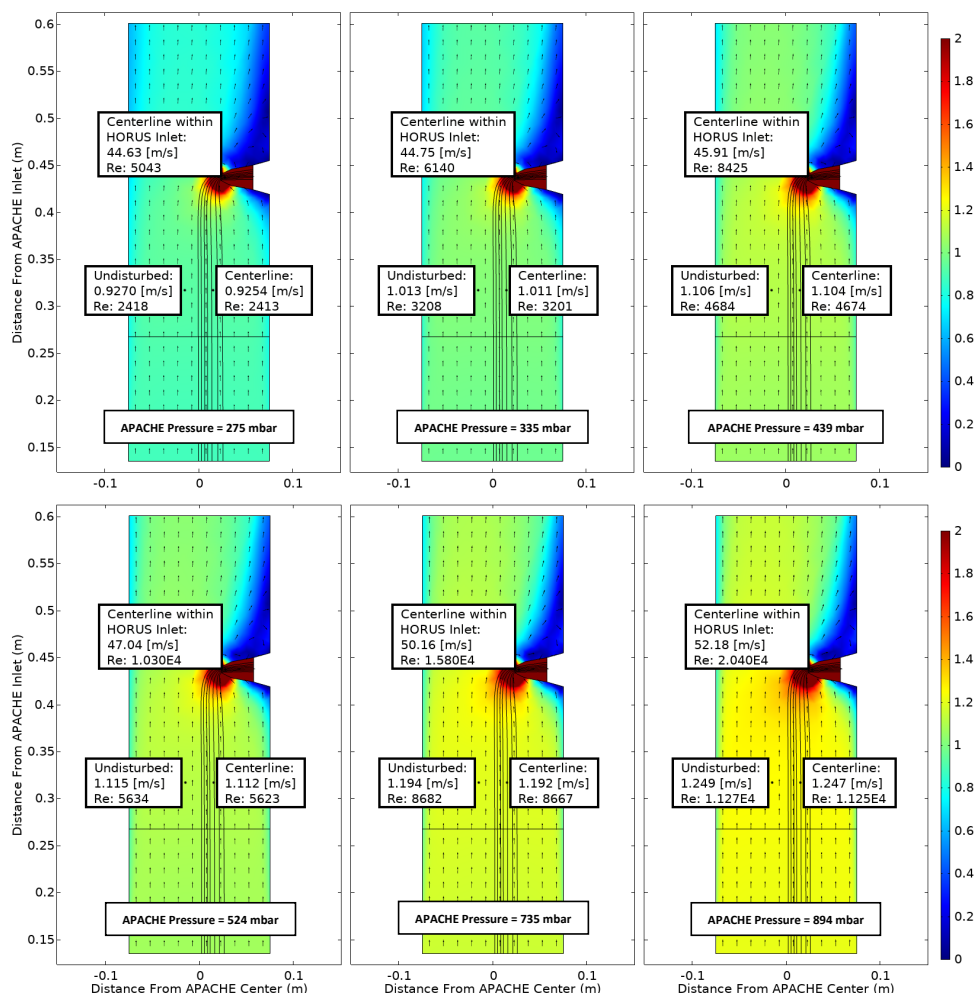
Figure 7. COMSOL Multiphysics output data, simulating the flow speed conditions at 6 discreet pressures within APACHE ranging from 275 to 894 mbar, between the sintered filter and the first perforated stainless steel plate. The color represents flow speed in m s^{-1}. The black lines are the streamlines created by the HORUS sample flow. The black arrows depict the flow direction. The x-axis is the distance from the center of APACHE in meters. The y-axis is the distance from the APACHE inlet. The centerline within HORUS inlet tags show the flow conditions in the center of the fully formed flows after the HORUS pinhole, the undisturbed tags show the flow conditions outside of the HORUS streamlines, and the centerline tags show the flow conditions in the center of the streamlines (i.e. the area of flow influenced by HORUS sampling).

360

361 The L term represents OH mixing ratios on the left most streamline, C represents OH mixing
362 ratios in the center of the streamlines, and R represents OH mixing ratios on the right most
363 streamline. The mean mixing ratio at each APACHE pressure does not change significantly
364 and is thus independent of the distance from the lamp. Conversely, the standard deviations of
365 the OH mixing ratios within the HORUS sampling streamlines decrease as the distance from
366 the lamp increases, indicating that the air is homogenizing. However, figure 8 and table 2, with
367 support from available measurements, indicate that the OH-depleted air masses (i.e. air masses

368 that have experienced loss of OH at the APACHE walls) do not expand into and influence the
369 OH content of air that is being sampled by HORUS. The main loss process that influences
370 HO_X entering HORUS is the wall loss at the HORUS inlet itself. On average, 22.2 ($\pm$ 0.8) %
371 (1σ) of OH and HO_2 is lost at the inlet, which will form part of the α_{IPI} loss calculation in
372 section 5.

373
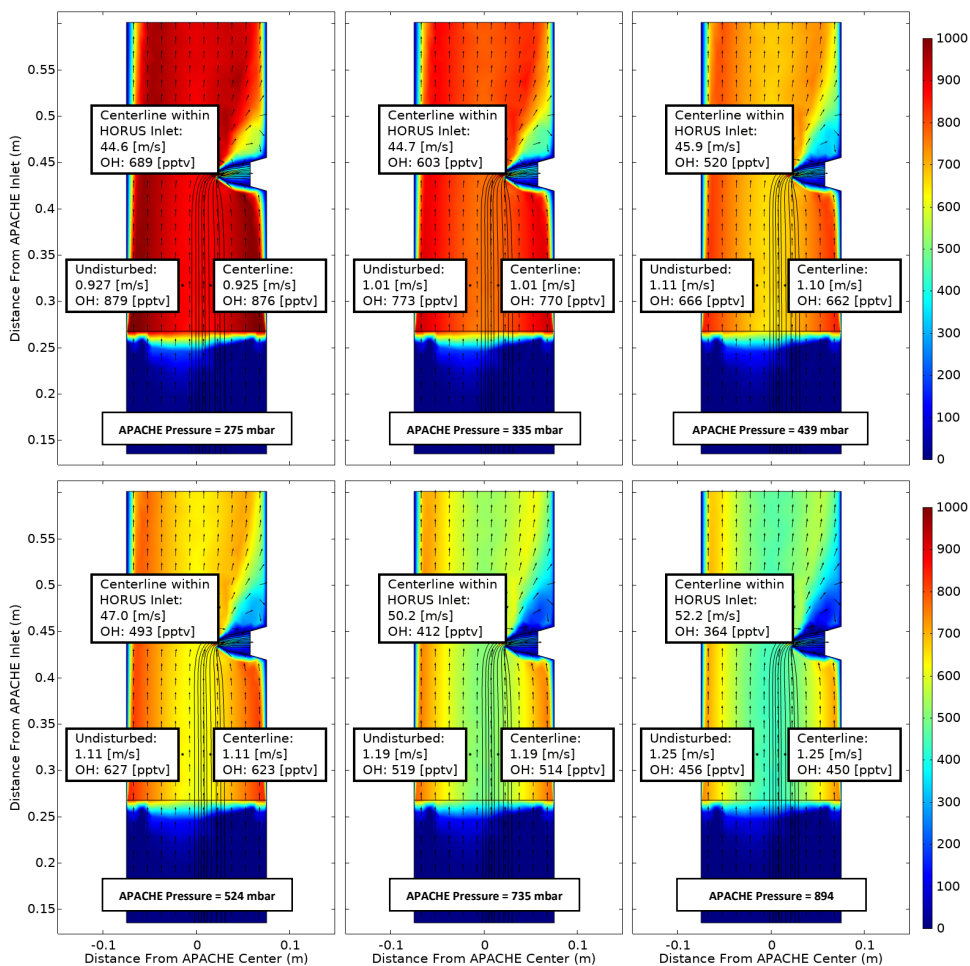
Figure 8. COMSOL Multiphysics output data, simulating OH conditions at 6 discreet pressures within
APACHE ranging from 275 to 894 mbar, between the sintered filter and the first perforated stainless steel
plate. The color is OH mixing ratio (pptv), with initial OH production occurring at the lamp (0.26 m from
APACHE inlet), using Eq. (7) and Eq. (8). The black lines are the streamlines created by the HORUS
sample flow. The black arrows depict the flow direction. The x-axis is the distance from the center of
APACHE in meters. The y-axis is the distance from the APACHE inlet. The centerline within HORUS
Inlet tags represent the flow and OH concentrations in the center of the fully formed flows after the
HORUS pinhole. The undisturbed tags show the flow conditions outside of the HORUS streamlines, and
the centerline tags show the flow conditions in the center of the streamlines (i.e. the area of flow
influenced by HORUS sampling).

Table 2. The evolution of OH within the HORUS sample flow streamlines, along the length of APACHE at all six pressures, within the streamlines created by HORUS sampling as depicted in figure 8. The L term represents OH mixing ratios on the left most streamlines, C represents OH mixing ratios in the center of the streamlines, and R represents OH mixing ratios on the right most streamline. The centerline within HORUS inlet column shows the OH mixing ratios in the center of the flow in the HORUS inlet. All standard deviations are quoted to 1σ.

APACHE Pressure (mbar)	OH (pptv) At the lamp					OH (pptv) 4.2 cm from lamp					OH (pptv) 8.4 cm from lamp					OH (pptv) 12.8 cm from lamp					OH (pptv) 2 cm before HORUS Inlet					In Centerline within HORUS Inlet
	L	C	R	Mean	Std (1σ)	L	C	R	Mean	Std (1σ)	L	C	R	Mean	Std (1σ)	L	C	R	Mean	Std (1σ)	L	C	R	Mean	Std (1σ)	
894	438	445	513	465	41.4	442	446	507	465	36.4	438	455	500	464	32.0	442	456	501	466	30.8	445	457	490	464	23.3	364
735	502	508	572	527	38.8	506	509	567	527	34.4	502	519	560	527	29.8	507	519	562	529	28.9	509	521	550	527	21.1	412
524	611	617	672	633	33.6	615	619	668	634	29.5	613	627	660	633	24.1	617	628	664	636	24.6	619	629	651	633	16.4	493
439	652	657	706	672	29.8	656	659	702	672	25.7	654	666	698	673	22.7	657	667	699	674	21.9	660	669	686	672	13.2	520
335	760	765	805	777	24.7	764	766	801	777	20.8	762	773	799	778	19.0	766	774	803	781	19.5	768	776	788	777	10.1	603
275	866	871	907	881	22.4	870	872	907	883	20.8	869	879	904	884	18.0	873	880	905	886	16.8	875	882	889	882	7.0	689

374

4.2 UV conditions

The photolysis lamp is housed in a mount with the side facing into the chamber having an anodized aluminum band with thirty 8 mm apertures installed between it and a quartz wall. The housing was flushed with pure nitrogen to purge any O_2 present before the lamp was turned on. The nitrogen flushing was kept on continuously thereafter. After approximately one hour, the lamp reached stable operation conditions, i.e the relative flux emitted by the lamp as measured by a photometer (seen in Figure 1b at the UVL on the underside of the APACHE chamber) was constant. The flux (F_β) entering APACHE is not the same as the flux experienced by the molecules sampled by HORUS (F). Factors influencing the ratio between F_β and F are as follows. (i) Absorption of light by O_2, which is particularly important as O_2 has a strong absorption band at 184.9 nm and the O_2 density changes in APACHE when calibrating at the different pressures. (ii) The variable radial flux, which is dependent on the geometric setup of the ring lamp and on the location within the irradiation cross section where the molecule is passing. These factors were resolved through the combination of two actinometrical crosscheck methods. The advantage of actinometrical methods is that the flux calculated is derived directly from the actual flux that is experienced by the molecules themselves as they pass through the APACHE chamber. Therefore, allowing direct calibration of the flux inside APACHE itself.

The first actinometrical method (A) used the ground based calibration device (Martinez et al., 2010) to calibrate the HORUS instrument to be used as a transfer standard. Only for the purpose of this experiment, the critical orifice diameter was changed from the airborne configuration of 1.4 mm to a 0.8 mm on-ground* configuration to adapt HORUS to the mass flow that the ground based calibration device is able to provide. The asterisk discerns terms that were quantified when the smaller 0.8 mm critical was used. The calculated instrument on-ground* sensitivity was then used to translate OH and HO_2 concentrations produced by the uv-technik Hg ring lamp into a value for F_β. Take note that for the calibrations discussed in section 5, the initial 1.4 mm diameter critical orifice used during the airborne campaign was re-installed.

The HORUS on-ground* sensitivity at 1010 mbar for OH and HO_2 are 12.79 ($\pm$ 1.8) and 16.59 ($\pm$ 2.3) cts pptv^{-1} mW^{-1} respectively, with the uncertainties quoted to 1σ. This sensitivity was then used to calculate the OH and HO_2 concentrations at the instrument inlet with the APACHE system installed and operating at 1010 mbar. To ensure sufficient flow stability during calibration at this high pressure, the Edwards GSX160 scroll pump was disengaged. Additionally, the water mixing ratios were kept constant (~3.1 mmol mol^{-1}) and oxygen levels were varied by adding different pure N_2 and synthetic air mixtures, via MFCs. The OH and HO_2 concentrations at the HORUS inlet were 1.51 ($\pm$ 0.01) and 1.43 ($\pm$ 0.01) x 10^{10} molecules cm^{-3} respectively when only pure synthetic air and water vapor were injected into APACHE, the uncertainties here are quoted as measurement variability at 1σ. Using these values, the OH and HO_2 concentrations at the lamp were back calculated accounting for radical-radical loss reactions (R6-R8) using rate constants taken from Burkholder et al. (2015) with temperature (T) in Kelvin.

$$OH + OH \rightarrow H_2O + O(^3P) \qquad k = 1.8 \times 10^{-12} \cdot \exp\left[\frac{1}{T}\right] \qquad (R6)$$

$$HO_2 + HO_2 \rightarrow H_2O_2 + O_2 \qquad k = 3.0 \times 10^{-13} \cdot \exp\left[\frac{460}{T}\right] \qquad (R7)$$

417   $OH + HO_2 \rightarrow H_2O + O_2$ $k = 4.8 \times 10^{-11} \cdot \exp^{\left[\frac{250}{T}\right]}$ (R8)
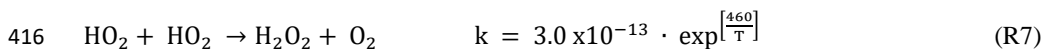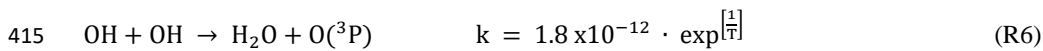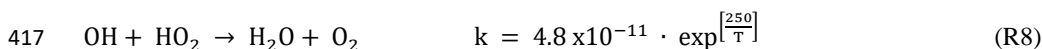
418   The chemical losses of OH and HO_2 were found to be 32 % and 30%, respectively, yielding
419   OH concentrations of 2.2 ($\pm$ 0.02) x 10^{10} molecules cm^{-3} and HO_2 concentrations of 2.0 ($\pm$
420   0.02) x 10^{10} molecules cm^{-3} at the lamp, at 1010 mbar, using a water vapor mixing ratio of 3.1
421   mmol mol^{-1} in pure synthetic air. The uncertainties are quoted as measurement variability at
422   1σ. The photon flux (F) experienced by the air sampled by HORUS, quantified using the OH
423   and HO_2 concentrations stated above, ranged from 3.75 x10^{14} photons cm^{-2} s^{-1} to 6.1 x10^{14}
424   photons cm^{-2} s^{-1} depending on oxygen concentrations and considering the chemical losses. As
425   described before, Eq.(7) shows how the production of OH at the lamp is calculated:

426   $[OH] = [H_2O] \cdot \sigma_{H_2O} \cdot F_{184.9\,nm} \cdot \phi_{H_2O} \cdot t$ (7)

427   $F_{184.9\,nm}$ *is* the absolute flux that is encountered by the water molecules as they pass across
428   the photolysis region, which is dependent on the attenuation of the flux (F_β) entering APACHE
429   due to water vapor and O_2 molecules. Whereas the absorption coefficient of water vapor is
430   constant across the linewidth of the 184.9 nm Hg emission line, the effective absorption cross
431   section of molecular oxygen (σ_{O2}) changes significantly at 184.9 nm within the linewidth of
432   the Hg lamp (Creasey et al., 2000). Therefore, σ_{O2} affecting the APACHE calibrations is
433   dependent on O_2 concentration, and the ring lamp temperature and current. Since the operating
434   temperature of the uv-technik Hg lamp and the current applied (0.8 A) was kept constant during
435   the actinometrical experiments and during the APACHE calibrations, any effect on σ_{O2}
436   regarding the ring lamp linewidth does not need to be investigated further in this study. The
437   relationship of $F_{184.9\,nm}$ to F_β can be derived using Beer-Lambert principles:

438   $F_{184.9\,nm} = F_\beta \cdot e^{-\left(\gamma_{H_2O}[H_2O]\, +\, \gamma_{O_2}[O_2]\right)}$ (8)

439   Where F_β is the flux intensity entering APACHE from ring lamp, with:

440   $\gamma_{O2} = R_\beta \cdot \omega \cdot \sigma_{O2}$ (9)

441   Where R_β is the radial distance of the sampled air parcel to the ring lamp of APACHE, ω a
442   correction factor replicating the integrated product of the absorption cross section and the
443   ring lamp's emission line as modified by the effect of the absorption of O_2 present in between
444   the lamp and the flight path of the sampled air, normalized by σ_{O2} is the effective cross section
445   of O_2. When combining Eq. (7) and Eq. (8) the OH concentration produced at the lamp is
446   quantified as:

447   $[OH] = [H_2O] \cdot \sigma_{H_2O} \cdot \phi_{H_2O} \cdot t \cdot F_\beta \cdot e^{-\left(\gamma_{H_2O}[H_2O]\, +\, \gamma_{O_2}[O_2]\right)}$ (10)

448   Eq. (10) can be rearranged to:

449   $\ln\left[\dfrac{[OH]}{([H_2O] \cdot \sigma_{H_2O})}\right] = \ln\left(F_\beta \cdot t \cdot \phi_{H_2O}\right) + \left(-\gamma_{H_2O} \cdot [H_2O] - \gamma_{O_2} \cdot [O_2]\right)$ (11)

450   Figure 9, shows the measured production of OH, (left side of Eq. (11)) plotted against
451   oxygen concentration. Given that the other terms within Eq. (11) are constant with regards to
452   changing oxygen levels, the plotted gradient of the linear regression in figure 9 yields γ_{O2} as a
453   function of oxygen concentration being 1.3 x 10^{-19} ($\pm$ 0.05 x10^{-19}) cm^3 $molecule^{-1}$.

454
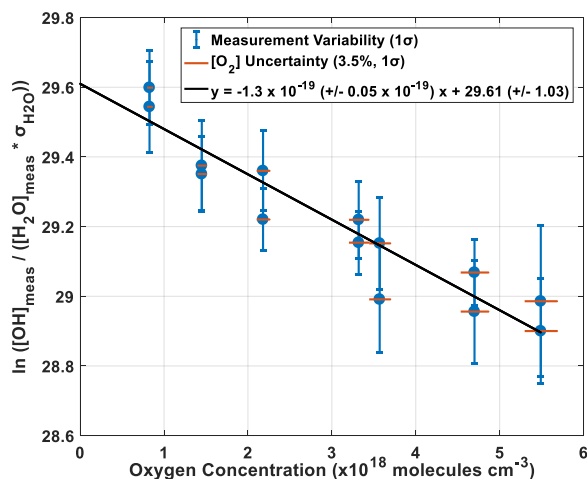
Figure 9. Plot showing the result of Eq. (11) as a function of oxygen concentration.

Given that, the y intercept of the linear regression, 29.61, is equal to the natural logarithm of (F_β t ϕ_{H_2O}), the flux entering APACHE F_β can be characterized:

$$F_\beta = \frac{e^{29.61}}{t \cdot \phi_{H2O}} = 6.9 \times 10^{14} \, (\pm 1.1 \times 10^{14}) \, s^{-1} \tag{12}$$

The accuracy in F_β from this method, which we call method A, is 15.9 % (1σ).

Table 3. Parameters and uncertainties involved in method A, using HORUS as a transfer standard. The total uncertainty is the sum of the quadrature of the individual uncertainties.

Parameter	Comments	Total Uncertainty 1σ (%)
NO Monitor (TEI)	Calibration uncertainty	5.2
NO standard (NPL)	Purity and concentration of the gas	1
N_2O cross section	JPL recommendation	2
H_2O cross section	JPL recommendation	2
γ_{O2}	From method A	3.5
$O(^1D)$ yield	Martinez et al. (2010)	1
Kinetic rate coefficients	JPL recommendation	12
F_β Variability	From method A	3.5
Photolysis chamber dimensions	Specifications of in-house workshop	3
[H_2O]	From calibration with NIST standard Dew point generator	2
[O_2]	From method A	3.4
Mass flow controllers	Calibration with NIST DryCal	2
Pressure and Temperature sensors	Validated against NIST standard	2
Overall Experimental Stability	Variability of measured terms	4
Overall uncertainty		15.9

The second actinometrical method (B) involved using an ANSYCO O3 41 M ozone monitor to measure the ozone mixing ratio profile between the HORUS inlet and the wall surface of APACHE, at ground pressure (1021 mbar). This method utilizes O_2 photolysis at 184.9 nm,

465   which produces two $O(^3P)$ atoms capable of reacting with a further two O_2 molecules to
466   produce O_3.

467    $O_2 + h\nu \rightarrow O(^3P) + O(^3P)$ (R9)

468    $O_2 + O(^3P) + M \rightarrow O_3 + M$ (R10)
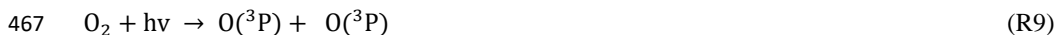
469   The value of 1.3×10^{-19} cm^3 $molecule^{-1}$ for γ_{O2} found in the previous method was used to
470   calculate the actinic flux entering APACHE:

471    $F_\beta = \dfrac{[O_3]}{[O_2] \cdot \gamma_{O_2} \cdot \phi_{O_2} \cdot t \cdot e^{-(\gamma_{O2}[O_2])}}$ (13)

472   Φ_{O2} is the quantum yield of O_2 at 184.9 nm, which has been determined to be 1 between
473   242 and 175 nm (Atkinson et al., 2004). As in method A, the ozone produced at the lamp is
474   quantified by back calculating from the ozone measured at the ANSYCO O3 41 M inlet
475   position. Typical ozone mixing ratios ranged from 45 – 72 ppb depending on the oxygen
476   concentration. From this approach, the calculated F_β is 5.7×10^{14} $(\pm 0.74 \times 10^{14})$ s^{-1} with a total
477   uncertainty of 12.9 % (1σ). From the combination of the two experiments, the final values
478   taken for the UV environment within APACHE are:

479   Actinic flux (F_β) = 6.3×10^{14} $(\pm 0.9 \times 10^{14})$ s^{-1}

480   Accuracy in F_β = 14.4 % (1σ)

481   **Table 4.** Parameters and uncertainties involved in Method B, using ANSYCO O3 41 M monitor. The total
482   uncertainty is the sum of the quadrature of the individual uncertainties.

Parameter	Comments	Total Uncertainty 1σ (%)
O_3 calibrator	Calibrated against a primary standard	2
$[O_3]$	Calibration of ANSYCO O3 41 M monitor	4
$[O_2]$	From method A	3.4
γ_{O2}	From method A	3.5
F_β Variability	From method A	3.5
Mass flow controllers	Calibration with NIST DryCal	2
Pressure and Temperature sensors	Validated against NIST standard	2
Experimental Stability	Variability of values	10.1
Overall uncertainty		12.9

483

484   **5   Results and discussion**

485   **5.1 Evaluation of instrumental sensitivity**

486   Figure 10 shows the sensitivity curve of HORUS, the quenching effect, the linear fits used
487   to quantify the pressure independent sensitivity coefficients, and relative HO_X transmission
488   values for OH , OH in the second axis, and HO_2 plotted as a function of the HORUS internal
489   density. Table 6 shows the pressure independent sensitivity coefficients for OH in the 1st axis,
490   OH in the 2nd axis, and HO_2 in the 2nd axis found from the slopes in figure 10 row C. As

491 described in section 3.2, the pressure driven wall losses in IPI and post critical orifice both
492 contribute to the overall sensitivity curve. The OH transmission terms (α_{IPI} and α_{HORUS}) can
493 be considered together as the total OH transmission (α_{Total}). According to the COMSOL
494 simulations, the losses of HO_X occur mainly at the inlet itself resulting in for both OH and HO_2
495 to be 78 (± 0.8, full range) %. To calculate the loss of HO_X within IPI, the following was used:

496 $$\alpha_{IPI\ OH} = 1 - \left\lceil \frac{OH_{DM}(P) \cdot t_{r\ IPI}\ (P,T) \cdot \pi}{IPI_A \cdot P_{IPI}} \right\rceil \tag{14}$$

497 $$\alpha_{IPI\ HO_2} = 1 - \left\lceil \frac{HO_{2\ DM}(P) \cdot t_{r\ IPI}\ (P,T) \cdot \pi}{IPI_A \cdot P_{IPI}} \right\rceil \tag{15}$$

498 Where t_{rIPI} is the transit time within IPI, i.e. the time it takes air to flow from the IPI inlet to
499 the critical orifice of HORUS. IPI_A is the internal cross sectional area of IPI and P_{IPI} is the
500 measured pressure within IPI. The OH_{DM} and $HO_{2\ DM}$ terms are the OH and HO_2 diffusion
501 coefficients as described in section 4.1.2. By applying Eq. (14) and Eq. (15), $\alpha_{IPI\ OH}$ and $\alpha_{IPI\ HO2}$
502 ranged from 0.98 to 0.995 and 0.99 to 0.997 respectively across the pressure range within IPI
503 of 210 – 1010 mbar and IPI transit times of 90 – 120 milliseconds. Summing the inlet wall
504 loss found from the COMSOL simulations (78 ± 0.8 %) and $\alpha_{IPI\ OH}$ and $\alpha_{IPI\ HO2}$ calculated from
505 Eq. (14) and Eq. (15) results in a combined α_{IPI} term for OH of 76.7 (± 2.2, full range) and for
506 HO_2 of 77.3 (± 1.6, full range). However, to calculate α_{Total}, the OH transmission post critical
507 orifice, α_{HORUS}, must be resolved. α_{HORUS} regarding OH and HO_2 can be calculated by adapting
508 Eq. (14) and Eq. (15) to the internal HORUS conditions producing:

509 $$\alpha_{HORUS\ OH} = 1 - \left\lceil \frac{OH_{DM}(P) \cdot t_{r1}\ (P,T) \cdot \pi}{HORUS_A \cdot P_{int}} \right\rceil \tag{16}$$

510 $$\alpha_{HORUS\ OH\_2} = 1 - \left\lceil \frac{OH_{DM}(P) \cdot t_{r2}\ (P,T) \cdot \pi}{HORUS_A \cdot P_{int}} \right\rceil \tag{17}$$

511 $$\alpha_{HORUS\ HO_2} = 1 - \left\lceil \frac{HO_{2\ DM}(P) \cdot t_{r2}\ (P,T) \cdot \pi}{HORUS_A \cdot P_{int}} \right\rceil \tag{18}$$

512 Where t_{r1} and t_{r2} are the transit times within HORUS from the critical orifice to the 1st and
513 2nd detection axis respectively. $HORUS_A$ is the internal cross sectional area of HORUS and P_{int}
514 is the measured internal pressure within HORUS. The OH transmission from the critical orifice
515 to the 1st detection cell ($\alpha_{HORUS\ OH}$) ranged from 0.84 to 0.96, the OH transmission from the
516 critical orifice to the 2nd detection cell ($\alpha_{HORUS\ OH\_2}$) ranged from 0.59 to 0.88, and the HO_2
517 transmission from the critical orifice to the 2nd detection cell ($\alpha_{HORUS\ HO2}$) ranged from 0.82 to
518 0.96. These ranges are quoted under the HORUS internal pressure range of 3.7 to 18.4 mbar
519 and internal transit times to the 1st detection axis (3.8 to 4.3 milliseconds) and 2nd detection
520 axis (23.5 to 27.8 milliseconds). The combined α_{Total} values for OH, OH at the second detection
521 axis, and HO_2 are plotted in figure 10 row D as a function of the internal density of HORUS.

522 The two actinometric methods used to calibrate the flux entering APACHE from the uv-
523 technik ring lamp, yielded encouraging and comparative results. The F_β found from ozone
524 actinometric method (5.7 ± 0.74 x 10^{14} s^{-1}) and from the HORUS transfer standard actinometric
525 method (6.9 ± 1.1 x 10^{14} s^{-1}) agree with the difference of 1.2 x 10^{14} s^{-1} representing only 60
526 % of the combined 1σ uncertainty in F_β, ± 2 x 10^{14} s^{-1} from the two methods.

527

528

5.2 Absolute Calibration Uncertainty

The contribution of parameter uncertainties to the respective sensitivities are summarized in tables 5 to 8.

Table 5. Parameters within APACHE, their ranges and uncertainties, contributing to the uncertainty in the three measurement sensitivities within HORUS.

Parameter (unit)	Range or typical value	Precision (1σ)	Total Uncertainty (1σ)
F_β at 184.9 nm (s^{-1})	6.3×10^{14}	3.5 %	14.4 %
σH_2O (cm^2 molecule^{-1})	7.22×10^{-20}	-	2 %
γ_{O2} (cm^3 molecule^{-1})	1.30×10^{-19}	1.8 %	3.5 %
$[O_2]$ ($\times 10^{18}$ molecules cm^{-3})	1.1 - 4.8	1.4 %	3.4 %
$[H_2O]$ ($\times 10^{16}$ molecules cm^{-3})	2.00 - 7.41	1.2 %	2 %
Mass flow controller (sL min^{-1})	203 - 988	< 2 %	2 %
Pressure sensors (mbar)	275 - 894	< 1 %	2 %
Temperature sensors (K)	282 - 302	< 1 %	2 %
Overall		5 %	16.2 %

Table 6. Pressure independent sensitivities and their overall uncertainty from calibrations with APACHE.

Parameter (cts cm^3 molecule^{-1} s^{-1})	Value	Precision ($\pm 1\sigma$)	Total Uncertainty (1σ)
c0 for OH in OH axis	1.44	4 %	6.9 %
c1 for OH in HO$_2$ axis	0.68	4 %	6.9 %
c2 for HO$_2$ in HO$_2$ axis	1.3	2 %	5.6 %

Table 7. Pressure dependent OH and HO$_2$ transmission and their overall uncertainty from calibrations with APACHE.

Parameter (%)	Value	Precision ($\pm 1\sigma$)	Total Uncertainty (1σ)
α_{Total} (for OH to OH axis)	61 - 72	2.8 %	14.3 – 11.4 %
α_{Total} (for OH to HO$_2$ axis)	35 - 65	4.3 %	14.1 – 11.5 %
α_{Total} (for HO$_2$ to HO$_2$ axis)	54 - 70	2.9 %	7.9 - 4.7 %

Table 8. Pressure dependent sensitivities for the three measurement within HORUS, their overall uncertainty from calibrations with APACHE. The range in the precision relates to the numbers quoted in the value column.

Parameter (unit)	Value	Precision ($\pm 1\sigma$)	Total Uncertainty (1σ)
C_{OH} (cts s^{-1} pptv^{-1} mW^{-1})	7.9 - 26.4	1.1 - 0.5 %	17.6 %
$C_{OH\,(2)}$ (cts s^{-1} pptv^{-1} mW^{-1})	3.9 - 10.5	2.0 - 0.3 %	17.6 %
C_{HO2} (cts s^{-1} pptv^{-1} mW^{-1})	7.5 - 22.3	0.4 - 0.7 %	17.1 %
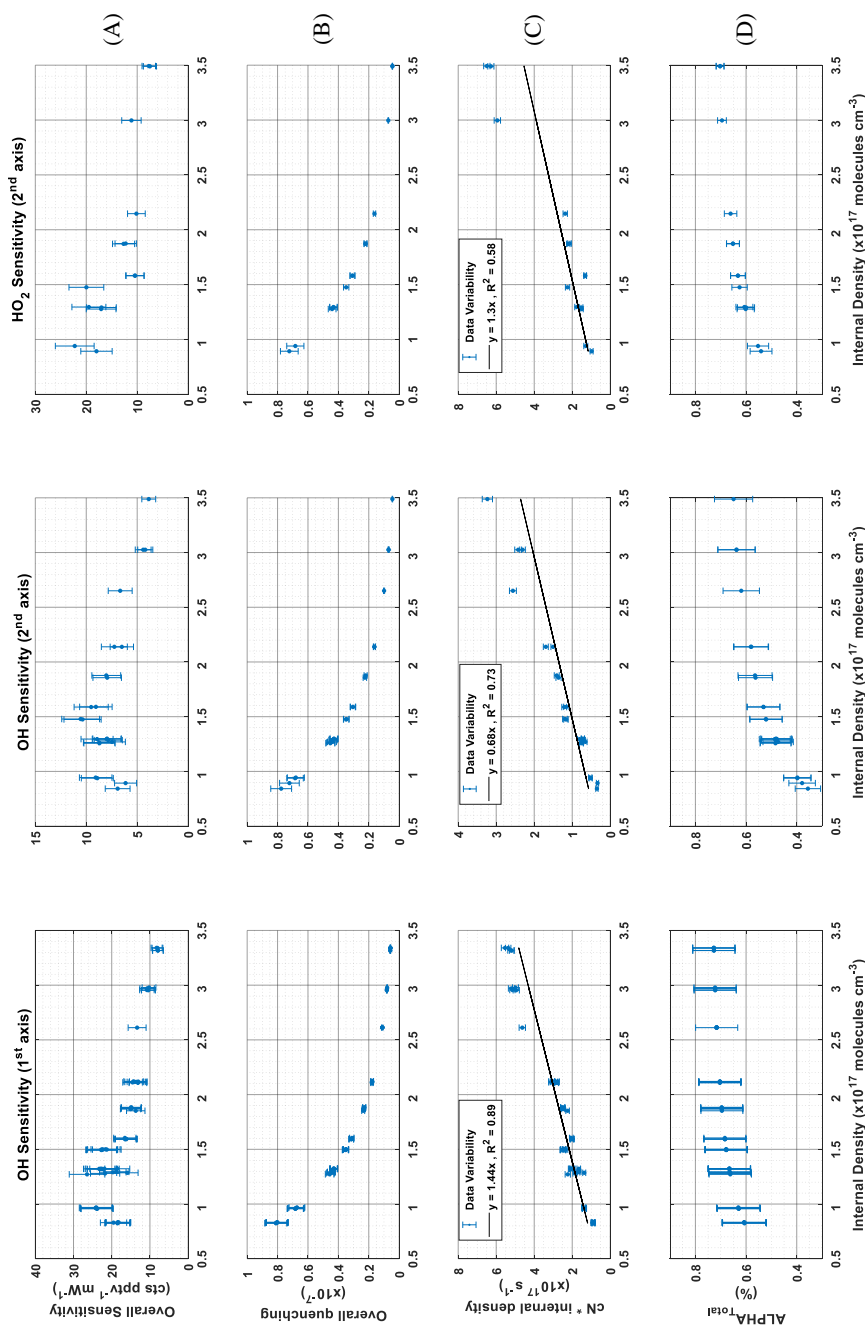
Figure 10. The determination of the pressure based sensitivity of OH in both axes and HO_2. The data shown are one-hour averages for the tested pressures, all plotted with the internal density on the x-axis. The top row (A) is the overall sensitivity curve, the second row (B) is internal quenching by N_2, O_2, and water vapor, and row (C) is internal density and cN (c0 for OH 1st axis, c1 for OH 2nd axis and c2 for HO_2), (D) is the total OH and HO_2 transmissions, all plotted against internal density. The error bars represent measurement variability (1σ), for rows B and C. In rows A and D, the error bars represent the total uncertainty (1σ).

542

6 Conclusions

The overall goal of this study was to develop and test a new calibration system capable of providing the high flows required by the airborne HORUS system whilst maintaining stable pressures across the pressure ranges experienced during flight. Such systems are critical to suitably characterize airborne systems, (such as a LIF-FAGE measuring HO_X), that have a strong pressure dependent sensitivity. In addition, this system is purely based on the use of water-vapor photolysis, which is a frequently adopted technique for HO_X instrument calibration (Martinez et al., 2003; Faloona et al., 2004; Dusanter et al., 2008). The COMSOL multiphysics simulations constrained by temperature, pressure and mass flow measurements demonstrated that air masses at the boundary of the APACHE system do not have sufficient time to expand into the streamlines created by the HORUS sample flow and influence the HO_X content entering HORUS. The main HO_X wall losses occurred at the HORUS inlet where on average 23.3 % ($\pm$ 1.6, full range) of OH and 22.7 % ($\pm$ 0.9, full range) of HO_2 are lost. While the application of these factors contribute to the uncertainty in the overall calibration factor, they proved to be critical in understanding and constraining the UV conditions within APACHE. The largest uncertainties result from constraining the flux (F_β) entering APACHE (6.3 $\pm$ 0.9 x 10^{14} s^{-1} , 1σ) and the total uncertainty in the pressure independent sensitivity coefficients (ranging from 5.6 to 6.9 %, 1σ). The two actinometrical methods used to derive F_β proved to be in good agreement with one another, with the HORUS transfer standard method yielding 6.9 $\pm$ 1.1 x 10^{14} s^{-1} (1σ) and the ozone monitor method yielding 5.7 $\pm$ 0.74 x 10^{14} s^{-1} (1σ). Furthermore, the APACHE system enabled the total OH and HO_2 pressure dependent transmission factors to be characterized as a function of internal pressure using both COMSOL simulations and calculations of HO_X diffusivity to the walls within IPI and the low-pressure regime within HORUS. Overall, the APACHE calibration system sufficiently able to calibrate the airborne HORUS system across the pressure range experienced during flight. The relatively low overall uncertainty of 17 - 18 % (1σ) demonstrates the suitability of this calibration approach, particularly when compared to other calibration methods described earlier.

Author contributions. K.H, C.E, M.M, H.H, U.J, and M.R formulated the original concept and designed the APACHE system. D.M, H.H, and U.J prototyped, developed, and characterized the APACHE system. T.K, D.M, and H.H developed and performed the CFD simulations. D.M prepared the manuscript with contributions from all coauthors.

Acknowledgments. We would like to take this opportunity to give a thank you to the in-house workshop at the Max Planck Institute for Chemistry for construction and guidance in the development of APACHE. Additionally, a special thank you to Dieter Scharffe for his assistance and advice during the development stage of this project.

585 **References**

586

587 Albrecht, S. R., A. Novelli, A. Hofzumahaus, S. Kang, Y. Baker, T. Mentel, A. Wahner and H. Fuchs,
588   "Measurements of hydroperoxy radicals (HO2) at atmospheric concentrations using bromide
589   chemical ionisation mass spectrometry." Atmospheric Measurement Techniques **12,**2: 891-
590   902, 2019.
591 Atkinson, R., D. L. Baulch, R. A. Cox, J. N. Crowley, R. F. Hampson, R. G. Hynes, M. E. Jenkin, M. J. Rossi
592   and J. Troe, "Evaluated kinetic and photochemical data for atmospheric chemistry: Volume I -
593   gas phase reactions of O-x, HOx, NOx and SOx species." Atmospheric Chemistry and Physics **4**:
594   1461-1738, 2004.
595 Brauers, T., U. Aschmutat, U. Brandenburger, H. P. Dorn, M. Hausmann, M. Hessling, A. Hofzumahaus,
596   F. Holland, C. PlassDulmer and D. H. Ehhalt, "Intercomparison of tropospheric OH radical
597   measurements by multiple folded long-path laser absorption and laser induced fluorescence."
598   Geophysical Research Letters **23,**18: 2545-2548, 1996.
599 Brauers, T., M. Hausmann, A. Bister, A. Kraus and H. P. Dorn, "OH radicals in the boundary layer of the
600   Atlantic Ocean 1. Measurements by long-path laser absorption spectroscopy." Journal of
601   Geophysical Research-Atmospheres **106,**D7: 7399-7414, 2001.
602 Brune, W. H., P. S. Stevens and J. H. Mather, "Measuring OH and HO2 in the Troposphere by Laser-
603   Induced Fluorescence at Low-Pressure." Journal of the Atmospheric Sciences **52,**19: 3328-
604   3336, 1995.
605 Burkholder, J. B., S. P. Sander, J. Abbatt, J. R. Barker, R. E. Huie, C. E. Kolb, M. J. Kurylo, V. L. Orkin, D.
606   M. Wilmouth and P. H. Wine, "Chemical Kinetics and Photochemical Data for Use in
607   Atmospheric Studies, Evaluation No. 18." JPL Publication 15-10, 2015.
608 COMSOL, Multiphysics Documentation, version 5.4, [software], 2019.
609 Creasey, D. J., G. E. Evans, D. E. Heard and J. D. Lee, "Measurements of OH and HO2 concentrations in
610   the Southern Ocean marine boundary layer." Journal of Geophysical Research-Atmospheres
611   **108,**D15, 2003.
612 Creasey, D. J., D. E. Heard and J. D. Lee, "Absorption cross-section measurements of water vapour and
613   oxygen at 185 nm. Implications for the calibration of field instruments to measure OH, HO2
614   and RO2 radicals." Geophysical Research Letters **27,**11: 1651-1654, 2000.
615 Dilecce, G., P. F. Ambrico and S. De Benedictis, "An ambient air RF low-pressure pulsed discharge as
616   an OH source for LIF calibration." Plasma Sources Science & Technology **13,**2: 237-244, 2004.
617 Dorn, H. P., R. Neuroth and A. Hofzumahaus, "Investigation of OH Absorption Cross-Sections of
618   Rotational Transitions in the a(2)Sigma(+), V'=0 [- X(2)Pi, V''=0 Band under Atmospheric
619   Conditions - Implications for Tropospheric Long-Path Absorption-Measurements." Journal of
620   Geophysical Research-Atmospheres **100,**D4: 7397-7409, 1995.
621 Dusanter, S., D. Vimal and P. S. Stevens, "Technical note: Measuring tropospheric OH and HO2 by laser-
622   induced fluorescence at low pressure. A comparison of calibration techniques." Atmospheric
623   Chemistry and Physics **8,**2: 321-340, 2008.
624 Engel, V., V. Staemmler, R. L. Vanderwal, F. F. Crim, R. J. Sension, B. Hudson, P. Andresen, S. Hennig,
625   K. Weide and R. Schinke, "Photodissociation of Water in the 1st Absorption-Band - a Prototype
626   for Dissociation on a Repulsive Potential-Energy Surface." Journal of Physical Chemistry **96,**8:
627   3201-3213, 1992.
628 Faloona, I. C., D. Tan, R. L. Lesher, N. L. Hazen, C. L. Frame, J. B. Simpas, H. Harder, M. Martinez, P. Di
629   Carlo, X. R. Ren and W. H. Brune, "A laser-induced fluorescence instrument for detecting
630   tropospheric OH and HO2: Characteristics and calibration." Journal of Atmospheric Chemistry
631   **47,**2: 139-167, 2004.
632 Fuchs, H., B. Bohn, A. Hofzumahaus, F. Holland, K. D. Lu, S. Nehr, F. Rohrer and A. Wahner, "Detection
633   of HO2 by laser-induced fluorescence: calibration and interferences from RO2 radicals."
634   Atmospheric Measurement Techniques **4,**6: 1209-1225, 2011.

635 Fuchs, H., Z. F. Tan, A. Hofzumahaus, S. Broch, H. P. Dorn, F. Holland, C. Kunstler, S. Gomm, F. Rohrer,
636   S. Schrade, R. Tillmann and A. Wahner, "Investigation of potential interferences in the
637   detection of atmospheric ROx radicals by laser-induced fluorescence under dark conditions."
638   Atmospheric Measurement Techniques **9,**4: 1431-1447, 2016.
639 Hard, T. M., L. A. George and R. J. O'brien, "Fage Determination of Tropospheric OH and HO$_2$." Journal
640   of the Atmospheric Sciences **52,**19: 3354-3372, 1995.
641 Hard, T. M., L. A. George and R. J. O'Brien, "An absolute calibration for gas-phase hydroxyl
642   measurements." Environmental Science & Technology **36,**8: 1783-1790, 2002.
643 Heard, D. E. and M. J. Pilling, "Measurement of OH and HO2 in the troposphere." Chemical Reviews
644   **103,**12: 5163-5198, 2003.
645 Hens, K., A. Novelli, M. Martinez, J. Auld, R. Axinte, B. Bohn, H. Fischer, P. Keronen, D. Kubistin, A. C.
646   Nolscher, R. Oswald, P. Paasonen, T. Petaja, E. Regelin, R. Sander, V. Sinha, M. Sipila, D.
647   Taraborrelli, C. T. Ernest, J. Williams, J. Lelieveld and H. Harder, "Observation and modelling
648   of HOx radicals in a boreal forest." Atmospheric Chemistry and Physics **14,**16: 8723-8747,
649   2014.
650 Hofzumahaus, A., T. Brauers, U. Aschmutat, U. Brandenburger, H. P. Dorn, M. Hausmann, M. Hessling,
651   F. Holland, C. PlassDulmer, M. Sedlacek, M. Weber and D. H. Ehhalt, "The measurement of
652   tropospheric OH radicals by laser-induced fluorescence spectroscopy during the POPCORN
653   field campaign and Intercomparison of tropospheric OH radical measurements by multiple
654   folded long-path laser absorption and laser induced fluorescence - Reply." Geophysical
655   Research Letters **24,**23: 3039-3040, 1997.
656 Holland, F., M. Hessling and A. Hofzumahaus, "In-Situ Measurement of Tropospheric Oh Radicals by
657   Laser-Induced Fluorescence - a Description of the Kfa Instrument." Journal of the Atmospheric
658   Sciences **52,**19: 3393-3401, 1995.
659 Holland, F., A. Hofzumahaus, R. Schafer, A. Kraus and H. W. Patz, "Measurements of OH and HO2
660   radical concentrations and photolysis frequencies during BERLIOZ." Journal of Geophysical
661   Research-Atmospheres **108,**D4, 2003.
662 Ivanov, A. V., S. Trakhtenberg, A. K. Bertram, Y. M. Gershenzon and M. J. Molina, "OH, HO2, and ozone
663   gaseous diffusion coefficients." Journal of Physical Chemistry A **111,**9: 1632-1637, 2007.
664 Kukui, A., G. Ancellet and G. Le Bras, "Chemical ionisation mass spectrometer for measurements of
665   OH and Peroxy radical concentrations in moderately polluted atmospheres." Journal of
666   Atmospheric Chemistry **61,**2: 133-154, 2008.
667 Lelieveld, J., W. Peters, F. J. Dentener and M. C. Krol, "Stability of tropospheric hydroxyl chemistry."
668   Journal of Geophysical Research-Atmospheres **107,**D23, 2002.
669 Mallik, C., L. Tomsche, E. Bourtsoukidis, J. N. Crowley, B. Derstroff, H. Fischer, S. Hafermann, I. Huser,
670   U. Javed, S. Kessel, J. Lelieveld, M. Martinez, H. Meusel, A. Novelli, G. J. Phillips, A. Pozzer, A.
671   Reiffs, R. Sander, D. Taraborrelli, C. Sauvage, J. Schuladen, H. Su, J. Williams and H. Harder,
672   "Oxidation processes in the eastern Mediterranean atmosphere: evidence from the modelling
673   of HOx measurements over Cyprus." Atmospheric Chemistry and Physics **18,**14: 10825-10847,
674   2018.
675 Mao, J., X. Ren, L. Zhang, D. M. Van Duin, R. C. Cohen, J. H. Park, A. H. Goldstein, F. Paulot, M. R. Beaver,
676   J. D. Crounse, P. O. Wennberg, J. P. DiGangi, S. B. Henry, F. N. Keutsch, C. Park, G. W. Schade,
677   G. M. Wolfe, J. A. Thornton and W. H. Brune, "Insights into hydroxyl measurements and
678   atmospheric oxidation in a California forest." Atmospheric Chemistry and Physics **12,**17: 8009-
679   8020, 2012.
680 Martinez, M., H. Harder, T. A. Kovacs, J. B. Simpas, J. Bassis, R. Lesher, W. H. Brune, G. J. Frost, E. J.
681   Williams, C. A. Stroud, B. T. Jobson, J. M. Roberts, S. R. Hall, R. E. Shetter, B. Wert, A. Fried, B.
682   Alicke, J. Stutz, V. L. Young, A. B. White and R. J. Zamora, "OH and HO2 concentrations, sources,
683   and loss rates during the Southern Oxidants Study in Nashville, Tennessee, summer 1999."
684   Journal of Geophysical Research-Atmospheres **108,**D19, 2003.

685   Martinez, M., H. Harder, D. Kubistin, M. Rudolf, H. Bozem, G. Eerdekens, H. Fischer, T. Klupfel, C. Gurk,
686   R. Konigstedt, U. Parchatka, C. L. Schiller, A. Stickler, J. Williams and J. Lelieveld, "Hydroxyl
687   radicals in the tropical troposphere over the Suriname rainforest: airborne measurements."
688   Atmospheric Chemistry and Physics **10,**8: 3759-3773, 2010.
689   Mather, J. H., P. S. Stevens and W. H. Brune, "OH and HO2 measurements using laser-induced
690   fluorescence." Journal of Geophysical Research-Atmospheres **102,**D5: 6427-6436, 1997.
691   Novelli, A., K. Hens, C. T. Ernest, D. Kubistin, E. Regelin, T. Elste, C. Plass-Dulmer, M. Martinez, J.
692   Lelieveld and H. Harder, "Characterisation of an inlet pre-injector laser-induced fluorescence
693   instrument for the measurement of atmospheric hydroxyl radicals." Atmospheric
694   Measurement Techniques **7,**10: 3413-3430, 2014.
695   Regelin, E., H. Harder, M. Martinez, D. Kubistin, C. T. Ernest, H. Bozem, T. Klippel, Z. Hosaynali-Beygi,
696   H. Fischer, R. Sander, P. Jockel, R. Konigstedt and J. Lelieveld, "HOx measurements in the
697   summertime upper troposphere over Europe: a comparison of observations to a box model
698   and a 3-D model." Atmospheric Chemistry and Physics **13,**21: 10703-10720, 2013.
699   Ren, X. R., H. Harder, M. Martinez, R. L. Lesher, A. Oliger, J. B. Simpas, W. H. Brune, J. J. Schwab, K. L.
700   Demerjian, Y. He, X. L. Zhou and H. G. Gao, "OH and HO2 chemistry in the urban atmosphere
701   of New York City." Atmospheric Environment **37,**26: 3639-3651, 2003.
702   Roach, P. E., "The Generation of Nearly Isotropic Turbulence by Means of Grids." International Journal
703   of Heat and Fluid Flow **8,**2: 82-92, 1987.
704   Sander, S. P., B. J. Finlayson-Pitts, R. R. Friedl, D. M. Golden, R. E. Huie, C. E. Kolb, M. J. Kurylo, M. J.
705   Molina, G. K. Moortgat, V. L. Orkin and A. R. Ravishankara, "Chemical Kinetics and
706   Photochemical Data for Use in Atmospheric Studies." JPL Publication 02-25, 2003.
707   Schlosser, E., B. Bohn, T. Brauers, H. P. Dorn, H. Fuchs, R. Haseler, A. Hofzumahaus, F. Holland, F.
708   Rohrer, L. O. Rupp, M. Siese, R. Tillmann and A. Wahner, "Intercomparison of two hydroxyl
709   radical measurement techniques at the atmosphere simulation chamber SAPHIR." Journal of
710   Atmospheric Chemistry **56,**2: 187-205, 2007.
711   Schlosser, E., T. Brauers, H. P. Dorn, H. Fuchs, R. Haseler, A. Hofzumahaus, F. Holland, A. Wahner, Y.
712   Kanaya, Y. Kajii, K. Miyamoto, S. Nishida, K. Watanabe, A. Yoshino, D. Kubistin, M. Martinez,
713   M. Rudolf, H. Harder, H. Berresheim, T. Elste, C. Plass-Dulmer, G. Stange and U. Schurath,
714   "Technical Note: Formal blind intercomparison of OH measurements: results from the
715   international campaign HOxComp." Atmospheric Chemistry and Physics **9,**20: 7923-7948,
716   2009.
717   Sjostedt, S. J., L. G. Huey, D. J. Tanner, J. Peischl, G. Chen, J. E. Dibb, B. Lefer, M. A. Hutterli, A. J.
718   Beyersdorf, N. J. Blake, D. R. Blake, D. Sueper, T. Ryerson, J. Burkhart and A. Stohl,
719   "Observations of hydroxyl and the sum of peroxy radicals at Summit, Greenland during
720   summer 2003." Atmospheric Environment **41,**24: 5122-5137, 2007.
721   Smith, S. C., J. D. Lee, W. J. Bloss, G. P. Johnson, T. Ingham and D. E. Heard, "Concentrations of OH and
722   HO2 radicals during NAMBLEX: measurements and steady state analysis." Atmospheric
723   Chemistry and Physics **6**: 1435-1453, 2006.
724   Stevens, P. S., J. H. Mather and W. H. Brune, "Measurement of Tropospheric OH and HO$_2$ by Laser-
725   Induced Fluorescence at Low-Pressure." Journal of Geophysical Research-Atmospheres **99,**D2:
726   3543-3557, 1994.
727   Tang, M. J., R. A. Cox and M. Kalberer, "Compilation and evaluation of gas phase diffusion coefficients
728   of reactive trace gases in the atmosphere: volume 1. Inorganic compounds." Atmospheric
729   Chemistry and Physics **14,**17: 9233-9247, 2014.
730   Tanner, D. J. and F. L. Eisele, "Present OH Measurement Limits and Associated Uncertainties." Journal
731   of Geophysical Research-Atmospheres **100,**D2: 2883-2892, 1995.
732   Verreycken, T. and P. J. Bruggeman, "OH density measurements in nanosecond pulsed discharges in
733   atmospheric pressure N-2-H2O mixtures." Plasma Sources Science & Technology **23,**1, 2014.
734   Winiberg, F. A. F., S. C. Smith, I. Bejan, C. A. Brumby, T. Ingham, T. L. Malkin, S. C. Orr, D. E. Heard and
735   P. W. Seakins, "Pressure-dependent calibration of the OH and HO2 channels of a FAGE HOx

736   instrument using the Highly Instrumented Reactor for Atmospheric Chemistry (HIRAC)."
737   Atmospheric Measurement Techniques **8,**2: 523-540, 2015.
738   Zhang, D. H., M. A. Collins and S. Y. Lee, "First-principles theory for the H+H2O, D2O reactions." Science
739   **290,**5493: 961-963, 2000.

740

741